Research Article

Wearable PANI@$CoFe_2O_4$ organohydroges for strain sensing, EMI shielding and thermal insulation

Zhi Lei, Maoxia Lu, Daohai Zhang*, Dongju Liu, Yupeng Hu, Anmin Song, Junlei Wang, Wei Gong

School of Chemical Engineering of Guizhou Minzu University, Guiyang 550025, Guizhou, China.

Correspondence to: Prof. Daohai Zhang, School of Chemical Engineering of Guizhou Minzu University, Guiyang 550025, Guizhou, China. E-mail: zhangdaohai6235@163.com

How to cite this article: Lei, Z.; Lu, M.; Zhang, D.; Liu, D.; Hu, Y.; Song, A.; Wang, J.; Gong, W. Wearable PANI@$CoFe_2O_4$ organohydroges for strain sensing, EMI shielding and thermal insulation. *Soft Sci.* 2026;6:[Accepted]. http://dx.doi.org/10.20517/ss.2026.22

Received: 28 January 2026 | **Revised:** 15 March 2026 | **Accepted:** 26 March 2026

Abstract

With the rapid escalation of electromagnetic pollution and electromagnetic interference, conventional EMI shielding materials can no longer satisfy the integrated requirements of next-generation flexible electronic devices and information terminals for mechanical deformability, wearable adaptability, and real-time signal monitoring. In this work, a multifunctional PG/P@CoFe (PAM/Gly/PANI@$CoFe_2O_4$) composite organohydrogel sensor with synergistic electromagnetic dissipation was fabricated through a hydrothermal-assisted one-pot strategy. $CoFe_2O_4$ magnetic nanoparticles were first synthesized via an ethylene glycol-assisted solvothermal route. Subsequently, the surface-active sites of $CoFe_2O_4$ were utilized to induce aniline polymerization, yielding conductive-magnetic $CoFe_2O_4$ composite nanoparticles. Mechanical characterization demonstrated that the resulting organohydrogel exhibited excellent compressive properties, while the incorporation of glycerol effectively suppressed water evaporation and enhanced water-retention capability. Electromagnetic measurements revealed that, at a PANI@$CoFe_2O_4$ loading of 4 wt.%, the 4 mm-thick hydrogel achieved an electrical conductivity of 0.55 ± 0.1 S/m and an average electromagnetic interference shielding effectiveness (EMI SE) of 50.27 ± 2.51 dB in the X-band. In addition, the hydrogel exhibited excellent thermal iInsulation performance. More importantly, its outstanding adhesion and rapid stimuli-responsive behavior enabled favorable human–machine interactive strain-sensing performance with good compatibility. This work provides an effective strategy for the development of integrated, robust multifunctional materials that simultaneously combine flexible sensing, electromagnetic shielding, and thermal insulation.

Keywords: Multifunctional materials, hydrogels, electromagnetic shielding, wearable devices

Graphical Abstract

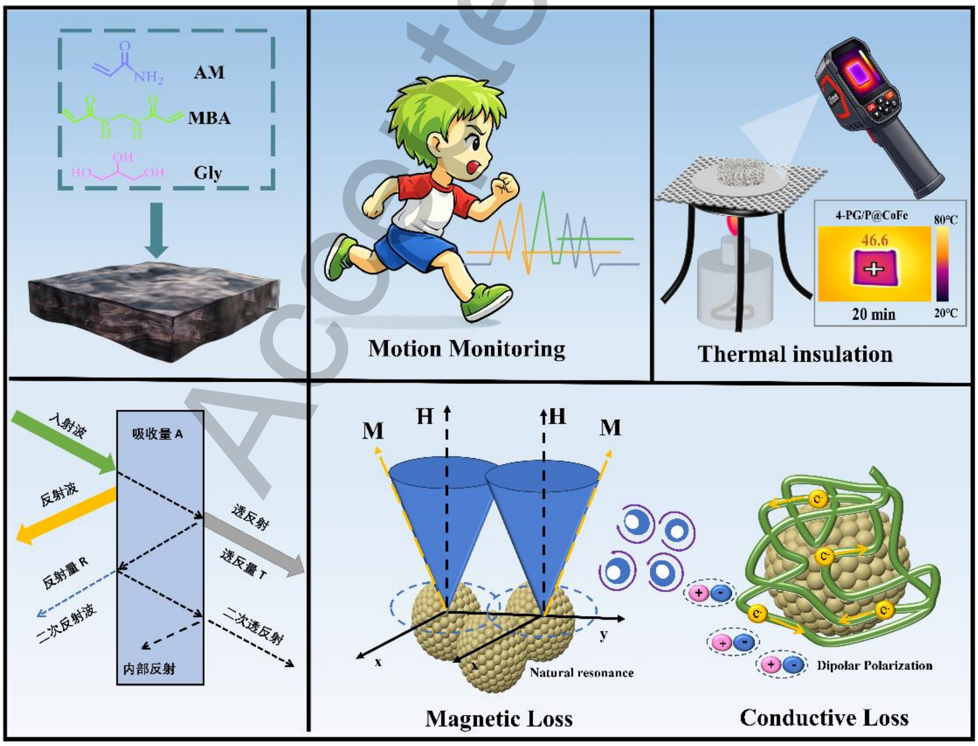

Highlights

1. A multifunctional PG/P@CoFe organohydrogel was fabricated via a

hydrothermal-assisted one-pot strategy.

2. *In situ* polymerized PANI uniformly coaed $CoFe_2O_4$, forming a stable conductive–magnetic synergistic network.

3. The organohydrogel exhibited high-sensitivity strain sensing together with favorable infrared stealth performance.

4. Absorption-dominated EMI shielding is achieved with an average SE of 50.27 dB in the X-band.

INTRODUCTION

With the rapid development of 5G communications, artificial intelligence, and aerospace technologies, the problems of electromagnetic pollution and electromagnetic interference have become increasingly serious, threatening the stable operation of precision electronic devices and raising potential concerns for human health[1-4]. Conventional electromagnetic shielding materials are primarily designed to attenuate incident electromagnetic waves. however, they are increasingly unable to satisfy the growing demand for lightweight design, flexibility, and multifunctional integration required by emerging applications such as internet-connected devices, wearable electronics, and health monitoring systems[5-7]. As electronic devices become increasingly miniaturized and sophisticated, and as their application scenarios become more complex, the development of EMI shielding materials must evolve toward multifunctional integration[8-10]. Owing to their lightweight nature, mechanical softness, inherent adhesiveness, and excellent compatibility with functional fillers, hydrogels have emerged as highly promising candidates for this purpose[11-13]. Through rational engineering of the polymeric network and precise regulation of functional fillers, their physicochemical properties and application-specific functionalities can be effectively tailored. By incorporating various conductive fillers, such as conductive polymers, carbon nanotubes, graphene, and metal-based materials, the electrical conductivity of hydrogels can be effectively regulated[14,15]. This unique combination has made hydrogels highly attractive for applications in flexible electronics, energy storage and sensing, while also offering a new framework for the development of multifunctional and integrated electromagnetic shielding materials. However, a critical challenge remains. Most conductive fillers exhibit poor dispersibility in hydrogel precursor solutions and tend to aggregate or sediment. Therefore, the rational selection and surface modification of functional fillers are crucial for constructing high-performance composite hydrogels.

Among various conducting polymers, polyaniline (PANI) has attracted extensive attention owing to its tunable oxidation states, high electrical conductivity, and capability for in situ polymerization in aqueous media[16]. However, pristine PANI exhibits strong hydrophobicity and limited hydrophilicity, resulting in poor solubility and unsatisfactory dispersibility in aqueous systems. In acidic media, protonation of the PANI molecular chains can markedly improve both its dispersibility and electrical conductivity[17,18]. Nevertheless, excessively high electrical conductivity can easily lead to discontinuous conductive pathways and a limited number of interfacial polarization sites, resulting in unsatisfactory electromagnetic wave attenuation performance[19]. Therefore, it is necessary to introduce other components to alleviate issues such as insufficient interfacial polarization. $CoFe_2O_4$ is a typical spinel-structured magnetic material and a ferrite that possesses high magnetic anisotropy, considerable magnetostrictive properties, and strong electromagnetic loss capability[20,21]. $CoFe_2O_4$ exhibits excellent thermochemical stability, enabling it to maintain its structural integrity without significant decomposition even under acidic, oxidizing, or high-temperature conditions[22-24]. Unfortunately, its electrical conductivity is inferior compared with that of many metal-based materials[25,26]. It is predominantly employed as a magnetic loss component rather than a highly conductive material in electromagnetic shielding and microwave absorption applications. Wang *et al.*[5] prepared the MXene/$CoFe_2O_4$ multifunctional hydrogel via a rapid gelation method, which not only addressed the issue of filler agglomeration but also improved the electrical conductivity of the hydrogel. The average EMI SE of this hydrogel in the X-band reaches 54.21 dB. Zhou *et al.*[27] prepared Fe_3O_4@RGO by a hydrothermal method, which resolved the problems of Fe_3O_4 precipitation and RGO stacking. They also fabricated the Fe_3O_4@RGO/PAM conductive hydrogel, whose maximum EMI SE is 27.1 dB. Diao *et al.*[11] optimized MXene layers via covalent organic frameworks (COFs) and successfully prepared MXene@COF heterostructured hydrogels, preventing MXene nanosheets from aggregation and self-stacking through the outer layer. The average EMI SE of this hydrogel is 32.01 dB. Thus, we can effectively overcome their respective defects by compounding PANI conductive materials and $CoFe_2O_4$ magnetic materials: On the one hand, the magnetic particles contribute magnetic loss mechanisms such as natural resonance and eddy current loss[20,28,29]. On the other hand, the interfaces between $CoFe_2O_4$ and PANI can induce dipole polarization and interfacial polarization, thereby enabling a synergistic multi-mechanism attenuation of electromagnetic waves[30,31]. More importantly, the integration of the conductive PANI network with magnetic $CoFe_2O_4$ nanoparticles facilitates the construction of a composite network that simultaneously exhibits dielectric and magnetic loss characteristics, thereby optimizing impedance matching and enhancing the overall microwave absorption efficiency. In addition, polyacrylamide (PAM), as a hydrophilic polymer network material, possesses excellent flexibility and a controllable porous structure, making it an ideal matrix for constructing composite hydrogels[32-34]. The incorporation of glycerol (Gly) not only significantly enhances the mechanical toughness and water-retention capability of the hydrogel, but also promotes internal energy dissipation and stabilizes the conductive network through hydrogen-bond interactions.

In this work, we successfully synthesized $CoFe_2O_4$ magnetic nanoparticles via a hydrothermal method. Owing to the abundant surface metal active sites (Co^{2+} and Fe^{3+}), surface hydroxyl groups (-OH), and oxygen vacancies, the nanoparticles exhibit a strong adsorption capability toward aniline[35]. The lone-pair electrons on the amino group of aniline can coordinate with Co^{2+} and Fe^{+}, enriching aniline at the $CoFe_2O_4$ surface and facilitating subsequent in situ oxidative polymerization. This interfacial coordination is the key to constructing conductive-magnetic PANI@ $CoFe_2O_4$ composite nanoparticles. Based on this mechanism, the homogeneous incorporation of PANI@$CoFe_2O_4$ into the PG (PAM/Gly) matrix enables the construction of a hierarchical conductive-magnetic synergistic network, thereby endowing the hydrogel with integrated EMI shielding, thermal insulation, and flexible strain-sensing properties.

EXPERIMENTAL

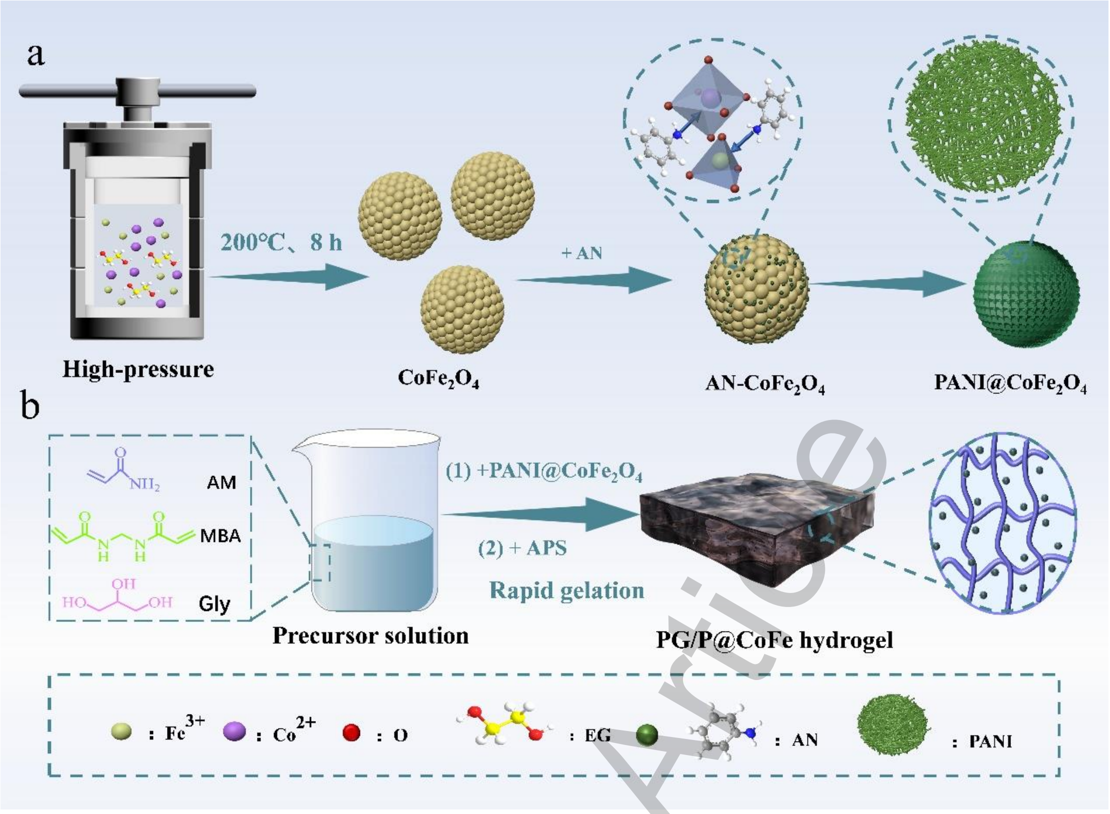

Figure 1. Preparation flowchart of the PG/P@CoFe hydrogel.

Experimental materials

Cobalt(II) chloride hexahydrate ($CoCl_2 \cdot 6H_2O$, reagent grade, 99.9%, molecular weight 291.03), ferric chloride hexahydrate ($FeCl_3 \cdot 6H_2O$, analytically pure, 99%, molecular weight 270.30), acrylamide (AM, analytically pure, 99.0%, molecular weight 71.08), ammonium persulfate (APS, analytically pure, 98%, molecular weight 228.20), N,N′-methylenebisacrylamide (MBA, 99%, molecular weight 154.17), sodium hydroxide (NaOH, analytically pure, 96.0%, molecular weight 40.00) were all purchased from Shanghai Aladdin Biochemical Technology Co., Ltd. Aniline (AN, ≥ 99.5%, molecular weight 93.13), hydrochloric acid (HCl, 36.5-38.0 wt.%, molecular weight 36.46) and ethylene glycol (EG, analytically pure, ≥ 98%, molecular weight 62.07) were purchased from Chongqing Chuandong Chemical Co., Ltd. Glycerol (Gly, analytically pure, ≥ 99.0%, molecular weight 92.09) was purchased from Xilong Scientific Co., Ltd.

Preparation of Conductive and Magnetic PANI@$CoFe_2O_4$ Nanoparticles

Take a certain mass of $CoCl_2 \cdot 6H_2O$ and $FeCl_3 \cdot 6H_2O$ and dissolve them sequentially in 45 mL of ethylene glycol to form solution a. Then dissolve NaOH in 50 mL of ethylene glycol to form solution b. Slowly add a to b while stirring magnetically in a 50°C water bath for 2 h; Next, react it in a reactor at 200 °C for 8 h. After centrifugation, washing, and drying, $CoFe_2O_4$ magnetic particles are obtained.

Disperse $CoFe_2O_4$ nanoparticles in 75 mL of deionized water, then add 0.1 mL of AN and stir for 20 min. Adjust the pH to 1 using HCl, then add the initiator APS. The mixture was stirred at 0-4 °C for 6 h, followed by centrifugation, washing, and drying to obtain PANI@$CoFe_2O_4$ conductive magnetic nanoparticles.

Preparation of PG/P@CoFe hydrogel

A specified amount of PANI@ $CoFe_2O_4$ was dispersed in 100 mL of deionized water and uniformly homogenized by mechanical stirring. Subsequently, 8 g of acrylamide (AM), 1.9 mL of glycerol (Gly), and 0.08 g of N,N′-methylenebisacrylamide (MBA) were sequentially introduced into the PANI@$CoFe_2O_4$ dispersion and thoroughly mixed. The polymerization initiator, ammonium persulfate (APS, 0.195 g), was then added to the mixture, and the resulting solution was transferred into a custom-designed mold for gelation. The obtained hydrogel was designated as X-PG/P@CoFe, where PG denotes the PAM/Gly network, and X indicates the weight percentage (%) of PANI@$CoFe_2O_4$ filler incorporated into the hydrogel.

Characterization and measurements

Sample microstructures were examined by scanning electron microscopy (SEM,ZEISS Sigma 300, Carl Zeiss AG). Chemical composition was analyzed via Fourier transform infrared spectroscopy (FT-IR, Nicolet iS50, Thermo Fisher Scientific) and X-ray photoelectron spectroscopy (XPS, Thermo Scientific K-Alpha, Thermo Fisher Scientific), and crystal structures were determined by X-ray diffraction (XRD, Rigaku Ultima IV, Suzhou Dehe Scientific Instrument Co., Ltd). Thermal behavior of the hydrogels was assessed using differential scanning calorimetry (DSC, Q10, TA Instruments), while compressive properties were measured with an electronic universal testing machine (GB/T 1041-2008, CMT6104, Mettler Industrial Systems (China) Co., Ltd.). Water absorption (Q) and retention (W) capacities were quantified according to Equations (1) and (2)[11].

$$Q=\frac{m_t\text{-}m_0}{m_0}\times 100\% \qquad (1)$$

$$W=\frac{w_t}{w_0}\times 100\% \qquad (2)$$

Here, m_t denotes the weight of the sample in its original state, m_0 denotes the weight of the sample in a dry state; w_t denotes the mass measured after exposure to air for t hours, and w_0 denotes the mass immediately upon reaching swelling equilibrium. Using a flexible strain sensor for sensitivity performance testing, the sensitivity coefficient (GF) is defined as the relative change in resistance (expressed as $(R\text{-}R_0)/R_0$, where R_0 and R represent the initial and real-time resistance) divided by the strain (ε). The electrical conductivity of the samples was determined using a standard four-probe resistance tester (FT-331). Using a vector network analyzer (N5225B, Keysight, Malaysia), the scattering parameters (S11, S12, S21, and S22), along with the complex permittivity and complex susceptibility used for analyzing EMI shielding characteristics. EMI shielding performance, including total SET, reflected SER, and absorbed SEA, as well as the coefficients for reflectance (R), absorptance (A), and transmittance (T), is calculated using the following Equations (3) to (8)[36,37].

$$R=|S_{11}|^2 \qquad (3)$$

$$T=|S_{21}|^2 \qquad (4)$$

$$A=1\text{-}T\text{-}R \qquad (5)$$

$$SE_R=10log\frac{1}{T} \qquad (6)$$

$$SE_A=10log\frac{1\text{-}R}{T} \qquad (7)$$

$$SE_T=SE_R+SE_A \qquad (8)$$

Statistical analysis

Normality was assessed using the Shapiro–Wilk test prior to parametric analysis.

Given the small sample size (*n* = 3), the data were considered approximately normally distributed. Descriptive statistics were calculated for all datasets. Quantitative data are expressed as mean ± standard deviation (SD). Comparisons between two groups were performed using an unpaired two-tailed t-test. Statistical significance was defined as $P < 0.05$. All statistical calculations were performed using Origin 2021.

RESULTS AND DISCUSSION

Synthesis mechanism and microstructure of PANI@$CoFe_2O_4$ and PG hydrogels

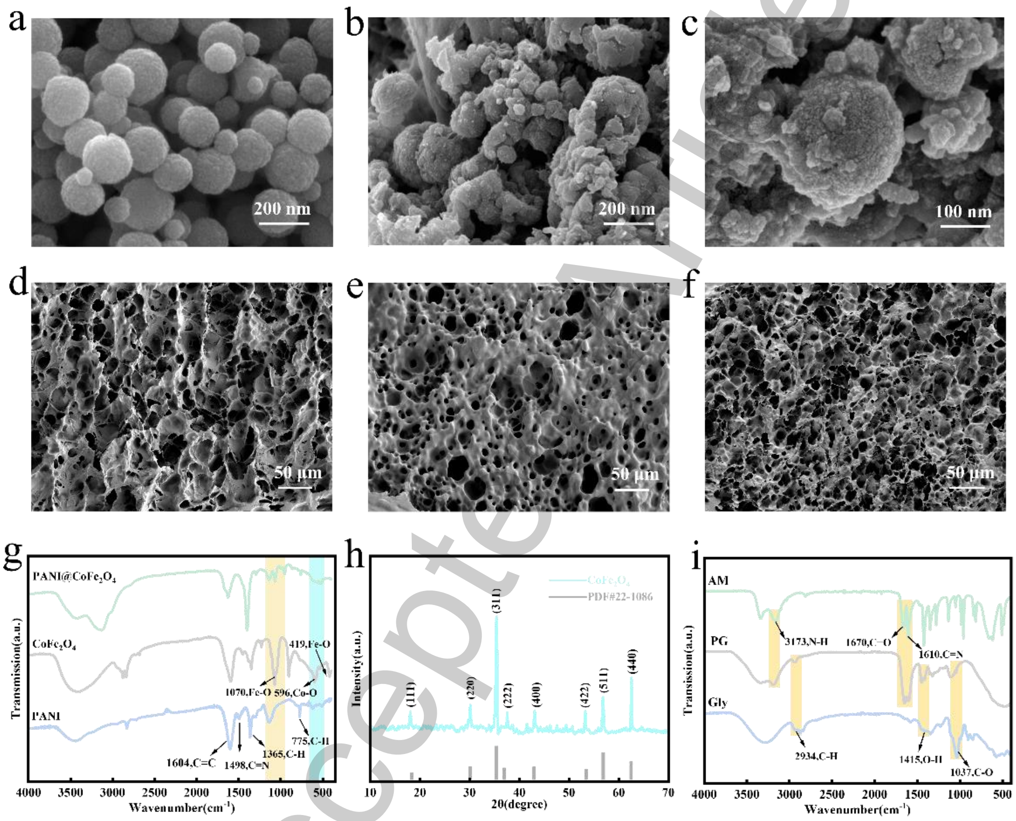

Figure 2. Microstructure and spectroscopic characterization of PANI@ $CoFe_2O_4$ and PG-based hydrogels. (b and c) SEM images of PANI@$CoFe_2O_4$. (d-f) SEM images of PG, 4-PG/PANI, and 4-PG/P@CoFe. (g) FTIR spectra of PANI, $CoFe_2O_4$, and PANI@ $CoFe_2O_4$. (h) XRD pattern of $CoFe_2O_4$. (i) FTIR spectrum of the PG hydrogel.

As illustrated in Figure 1a, ethylene glycol promoted the nucleation and crystal growth of $CoFe_2O_4$ and facilitated the formation of the spinel phase. The abundant surface metal-active sites of $CoFe_2O_4$ can coordinate with the amino nitrogen of aniline, thereby enriching aniline at the particle interface and favoring subsequent interfacial oxidative polymerization. Upon initiation by APS, aniline polymerized to form PANI, which coated the $CoFe_2O_4$ surface to yield the PANI@$CoFe_2O_4$ composite. Subsequently, as shown in Figure 1b, the composite was introduced into the Gly/PAM precursor solution and underwent in situ gelation, resulting in the formation of the PANI@$CoFe_2O_4$ hydrogel.

As shown in Figure 2a, the $CoFe_2O_4$ synthesized in ethylene glycol exhibits a relatively uniform spherical morphology. After compositing with PANI in the aqueous phase [Figure 2b and c], the $CoFe_2O_4$ particles were clearly encapsulated by a PANI coating layer. EDS elemental mapping and energy-dispersive spectroscopy analysis [Supplementary Figure 1] further confirmed the homogeneous distribution of C, N, Fe, and Co throughout the composite. Figure 2d-f shows the scanning electron microscopy image of the PG hydrogel, which exhibits a well-defined three-dimensional porous structure. When $CoFe_2O_4$ is introduced into the PG hydrogel, the pore structure of the hydrogel is disrupted [Figure 2e]. This phenomenon may be attributed to the aggregation and deposition of $CoFe_2O_4$ particles, which interact strongly with the polymer matrix. Such interactions lead to a tighter packing of the polymer chains, thereby reducing the size of the pore structures[38,39]. In contrast, when PANI@$CoFe_2O_4$ is incorporated, the pore structure becomes more abundant [Figure 2f]. The FTIR spectrum [Figure 2g] shows that the in situ polymerized PANI under acidic conditions exhibits a stretching vibration of the C=C bond at 1,604 cm^{-1}, a stretching vibration of the C-N bond at 1,498 cm^{-1}, and bending vibrations of the C-H bonds in the aromatic ring at 1,365 cm^{-1} and 775 cm^{-1}, as well as out-of-plane bending vibrations[40,41]. For $CoFe_2O_4$, the stretching vibration peaks of the Fe-O bonds appear at 419 cm^{-1} and 1,070 cm^{-1}, while the stretching vibration of the Co-O bond is observed at 596 cm^{-1}[42-44]. For the PANI@ $CoFe_2O_4$ composite material, the characteristic peaks at 1,070 cm^{-1} and 596 cm^{-1} remain, indicating that the Fe-O and Co-O bonds are still present in the composite. Additionally, the peaks corresponding to PANI can also be observed, indicating the successful integration of PANI with $CoFe_2O_4$. Meanwhile, at the same time, as shown in Figure 2h, the diffraction peaks corresponding to each crystal face in the spinel structure perfectly match those in the standard card (No. 22-1086)[45], confirming the successful synthesis of the $CoFe_2O_4$ spinel structure. PG organohydroges were prepared using glycerol (Gly) and acrylamide (AM) as matrix components. This process involves the free-radical polymerization of AM at 60 °C to form PAM[46].As shown in Supplemetnary Figure 2, PANI reduces the aggregation or sedimentation of $CoFe_2O_4$, enabling its uniform dispersion within the hydrogel, which helps promote the formation and stability of the hydrogel pore structure. In addition, FT-IR analysis of the PG hydrogel [Figure 2i] showed characteristic bands at 2,934, 1,415, and 1,037 cm^{-1}, corresponding to CH stretching, O-H bending, and C-O stretching vibrations of glycerol, respectively[47], confirming the successful construction of the PG hydrogel.

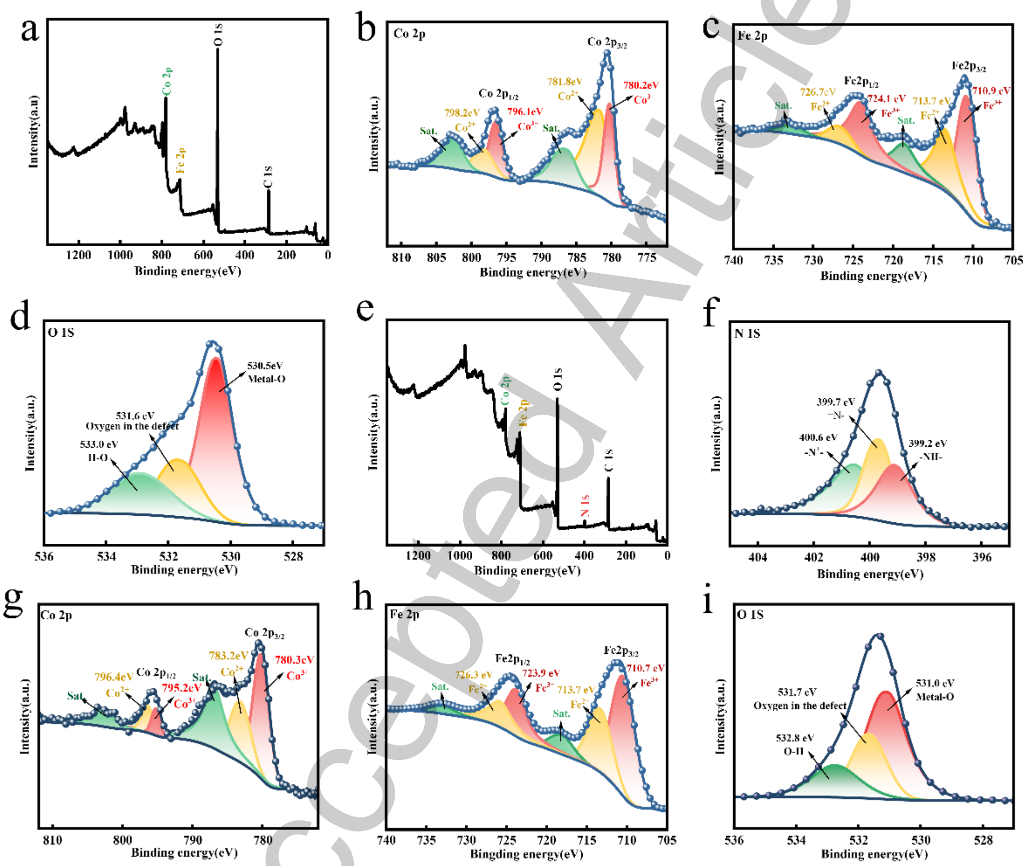

Figure 3. XPS characterization of $CoFe_2O_4$ and PANI@$CoFe_2O_4$. (a-d) Survey, Co 2p, Fe 2p, and O 1s spectra of $CoFe_2O_4$. (e-i) Survey, N 1s, Co 2p, Fe 2p, and O 1s spectra of PANI@$CoFe_2O_4$. XPS analysis (Fig. 3a) confirmed that spinel $CoFe_2O_4$ mainly consists of Co, Fe, and O, with no detectable impurities other than adventitious carbon. The high-resolution XPS spectra of Co 2p, Fe 2p, and O 1s are shown in Figure 3b-d. In Figure 3b, the two principal peaks at 780.5 and 796.6 eV are assigned to Co $2p_{3/2}$ and Co $2p_{1/2}$, respectively. The peaks at 780.2 and 796.1 eV correspond to Co^{+}, whereas those at 778.8 and 794.2 eV are attributed to Co^{2}[48,49]. The spectrum of Fe2p (Fig. 3c) shows characteristic peaks at binding energies of

711.0 eV and 724.7 eV, corresponding to Fe $2p_{3/2}$ and Fe $2p_{1/2}$. The peaks at 710.9 eV and 724.1 eV are attributed to Fe^{3+}, while the peaks at 713.7 eV and 726.7 eV correspond to Fe^{2+}[48,50] . The O 1s XPS spectrum exhibits three characteristic peaks [Figure 3d]. The peak at 530.5 eV corresponds to the metal-oxygen bonds, while the peak at 531.6 eV is assigned to defect oxygen. The peak at 533.0 eV arises from adsorbed water molecules on the surface of $CoFe_2O_4$[50,51]. When coated with PANI, as shown in Figure 3e, it is evident that the PANI@$CoFe_2O_4$ composite nanoparticles contain an additional N element. The N 1s spectrum [Figure 3f] shows three peaks at binding energies of 399.2 eV, 399.7 eV, and 400.6 eV, which are attributed to imine nitrogen (=N-), amine nitrogen (-NH-), and protonated nitrogen ($-N^+-$)[52]. The binding energies of Co, Fe, and O in PANI@$CoFe_2O_4$ do not exhibit significant shifts [Figure 3g-i], suggesting that no new covalent bonds were formed between PANI and $CoFe_2O_4$ and that the two components were mainly integrated through interfacial interactions.

Physical properties of the hydrogel

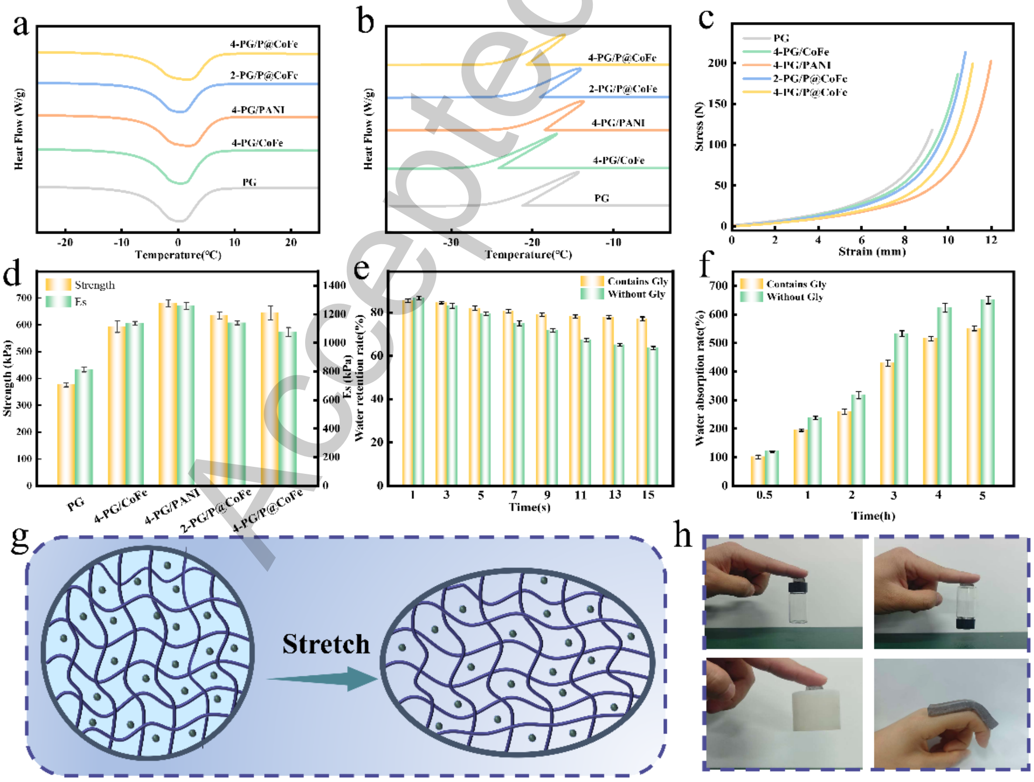

Figure 4. Physical properties of the hydrogels. (a and b) Crystallization and crystallization curves of the hydrogel. (c) Compression curve of hydrogel. (d) Compression strength and compression modulus of the hydrogel. (e-f) Effect of Gly

on the water retention and water absorption rates of the hydrogel. (g) Schematic of the semi-interpenetrating network changes of the hydrogel during stretching. (h) Images of the hydrogel's adhesion to different objects. Data are presented as mean ± SD (n = 3); error bars represent standard deviation. All photos in the figure were taken by the author during the experiment.

The melting and crystallization behaviors of the hydrogels were investigated by differential scanning calorimetry. As shown in Figure 4a and b, the incorporation of functional fillers induced slight variations in the melting and crystallization behaviors of the hydrogel, which can be attributed to their influence on the microcrystalline domains and chain packing of the polymer network. In terms of mechanical performance, PANI@$CoFe_2O_4$ acted as a multifunctional reinforcing filler, enhancing the mechanical properties of the organohydrogel through multiple interactions and structural effects. As shown in Figure 4c and d, the mechanical properties of the hydrogel were improved after incorporation of functional fillers. Among the samples investigated, the compressive strength (679.8 ± 13.60, n = 3) and modulus (1,258.9 ± 25.18, n = 3) of 4-PG/PANI hydrogel were significantly higher than those of PG hydrogel (376.3 ± 7.53 and 813.6 ± 16.27, n = 3, unpaired t-test, $P < 0.0001$, conformed to a normal distribution). Although both PANI and $CoFe_2O_4$ contributed to mechanical reinforcement, their strengthening mechanisms were different. The N- and O-containing functional groups on the PANI chains formed reversible physical crosslinking sites with the organohydrogel matrix, which helped maintain the integrity of the network under small deformation and partially dissociated or slid under large deformation to dissipate energy[19,53], thereby improving the elongation at break and toughness. In contrast, $CoFe_2O_4$ possesses a rigid structure with a mechanical modulus much higher than that of the soft polymer network. When uniformly dispersed within the hydrogel network, it can effectively bear and distribute external forces, thereby reducing local stress concentrations[54]. However, $CoFe_2O_4$ exhibits poor dispersibility within the hydrogel. Therefore, we introduced PANI onto its surface to overcome this limitation. When 4% PANI@$CoFe_2O_4$ filler is incorporated, the organohydrogel 4-PG/P@CoFe achieves a compressive strength (644.7 ± 25.89, n = 3) and modulus (1,076 ± 31.53, n = 3) that are significantly higher than those of PG hydrogel (376.3 ± 7.53 and 813.6 ± 16.27, n = 3, unpaired t-test, $P < 0.0001$, conformed to a normal distribution).The hydrogel's 3D cross-linked network structure not only endows it with excellent mechanical properties, such as toughness, elasticity, and fatigue resistance, but also ensures its outstanding water absorption and water retention capabilities. The storage of water molecules within its three-dimensional porous structure generally determines the stability of the hydrogel. Accordingly, the water retention capacity and water absorption performance of the glycerol-water binary system was quantitatively evaluated. Figure 4e demonstrates that the incorporation of glycerol exerts a significant enhancing effect on water retention capability. Under the same conditions, the hydrogel without glycerol exhibits a faster water loss rate than the glycerol-containing hydrogel. After 15 days of incubation under room temperature conditions, the water retention rate increases from 63.4 ± 0.75% to 77.1 ± 0.91%. Regarding the water absorption performance [Figure 4f], it can be observed that the hydrogel without glycerol exhibits a faster water uptake rate, indicating that water molecules permeate more rapidly in the glycerol-free system. Figure 4g shows a schematic diagram of the molecular chains moving relative to each other when the hydrogel is loaded. This further demonstrates that glycerol hinders the diffusion of water molecules. Therefore, the PG hydrogel can maintain its initial state and excellent performance over a longer period. Compared with conventional hydrogels, this improvement ensures the long-term preservation of structural integrity and functional performance. The surface of the PG/P@CoFe hydrogel contains abundant polar functional groups, enabling strong interfacial adhesion to various substrates, including biological tissues, inorganic glass, and plastics [Figure 4h]. Such robust adhesion provides a solid foundation for the integration of wearable sensors.

Electromagnetic shielding performance of the hydrogel

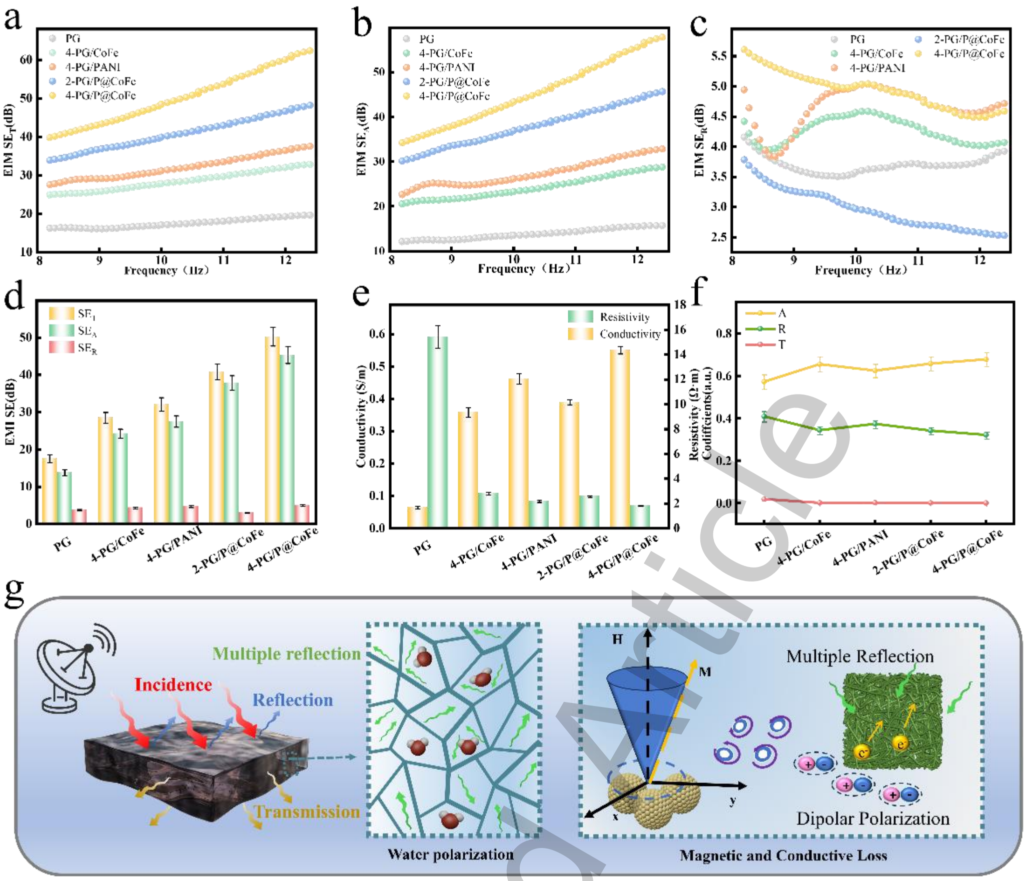

Figure 5. Electromagnetic shielding performance of the hydrogels. (a-c) Clearly illustrate the influence of frequency on the SET, SER, and SEA of the hydrogels. (d) Average SET, SER, and SEA values of hydrogels. (e) Electrical conductivity of the hydrogels. (f) T-R-A coefficients of the hydrogels. (g) Electromagnetic shielding mechanism of the hydrogels. Data are presented as mean ± SD (*n* = 3); error bars represent standard deviation.

In general, EMI shielding originates from reflection, absorption, and multiple internal reflections, which are associated with the responses of mobile charge carriers, electric dipoles, and internal interfaces/surfaces[55,56]. Moreover, the porous structure not only reduces the density of the material but also provides a large surface area and abundant accessible active sites. These active sites facilitate the scattering or multiple reflections of electromagnetic waves (EMWs), thereby promoting energy dissipation[57,58]. Meanwhile, the three-dimensional network structure increases the probability that the incident electromagnetic waves undergo multiple reflections and attenuation. As shown in Figures 5a-d, the hydrogels exhibit efficient and stable EMI shielding performance in the X-band, with the EMI shielding effectiveness increasing as the frequency rises. This variation can be attributed to several factors. (1) Enhanced dipole absorption: Water molecules possess a large permanent dipole moment, and under an alternating electromagnetic field, they undergo continuous orientational polarization. This process leads to stronger attenuation of interfering electromagnetic waves within the hydrogel, thereby dissipating the electromagnetic energy in the form of heat[57]. (2) Increased polarization relaxation: At higher frequencies, the electromagnetic field oscillates more rapidly, causing more frequent polarization relaxation of electric dipoles, which in turn enhances conduction loss[59]. More intense reflection and scattering: The shorter wavelengths associated with high-frequency electromagnetic waves interact more readily with the electric dipoles of water molecules and are more effectively reflected and scattered within the porous structure of the hydrogel, thereby generating greater energy dissipation[60]. As can be seen from Supplementary Figure 3, the electromagnetic shielding performance of hydrogels filled with the composite material formed by PANI and $CoFe_2O_4$ is superior to that filled with the two components separately. The reason is that PANI coating can reduce the sedimentation of $CoFe_2O_4$ at the bottom of the hydrogel. Although water has a strong ability to dissipate electromagnetic waves, the pure PG hydrogel cannot achieve a satisfactory SE value due to the absence of conductive and magnetic components. This indicates the necessity of incorporating conductive and magnetic components into the PG hydrogel to achieve high electromagnetic shielding performance. As shown in Figure 5e, the electrical conductivity of the hydrogel changes significantly after the incorporation of the composite material. The electrical conductivity (0.55 ± 0.01, $n = 3$) and compressive performance (50.27 ± 2.51, $n = 3$) of 4-PG/P@CoFe hydrogel were significantly higher than those of PG hydrogel (0.0648 ± 0.00389 and 17.51 ± 1.05, $n = 3$, unpaired t-test, $P < 0.0001$, conformed to a normal distribution). Although the PG/PANI hydrogel exhibits higher electrical conductivity than the 2-PG/P@CoFe hydrogel, its shielding performance relies primarily on free-electron reflection. Due to the absence of dielectric polarization, interfacial polarization, and magnetic loss-related absorption mechanisms, its overall shielding effectiveness remains limited[61]. In contrast, the 4-PG/P@CoFe hydrogel exhibits a moderately reduced conductivity while significantly enhancing impedance matching, dielectric loss, magnetic loss, and multiple scattering. This results in an absorption-dominated shielding mechanism, leading to electromagnetic shielding performance far superior to that of the 4-PG/PANI hydrogel. The present results suggest that simply increasing conductivity does not necessarily improve EMI shielding performance. A possible reason is that excessively high conductivity may deteriorate impedance matching, thereby increasing surface reflection[62]. As shown in Figure 5f, by analyzing the R, A and T coefficients, we can gain additional understanding of the shielding mechanism. It can be observed that the 4-PG/PANI hydrogel exhibits slightly higher R values than the other samples due to its relatively strong dielectric properties, which lead to increased impedance mismatch. More importantly, the T values of all hydrogels are close to zero, indicating their high efficiency in resisting electromagnetic interference[63,64]. Meanwhile, the A values are consistently higher than the R values, indicating that absorption is the dominant EMI shielding mechanism[65]. The schematic illustration of the electromagnetic shielding mechanism [Figure 5g] further demonstrates the EMI shielding process of the hydrogel. Table 1 Comparison of the electromagnetic shielding performance of this work with other multifunctional hydrogels[5,11,27,66-72].

Table 1. Comparison of the EMI shielding performance of representative hydrogels

Sample	**Thick (mm)**	**EMI SE**	**References**
MXene/CoFe$_2$O$_4$ hydrogel	5 mm	54.21 dB	[5]
MXene@COF hydrogel	3 mm	32.01	[11]
Fe$_3$O$_4$@RGO/PAM hydrogel	3 mm	27.10 dB	[27]
MXene Organohydrogel	4 mm	32.8 dB	[66]
MXene/gelatin hydrogel	3–5 mm	35–50 dB	[67]
MXene /PAM-CMC hydrogel	5 mm	46.3 dB	[68]
PVA-ANF/MXene@Ga hydrogel	/	35.7 dB	[69]
PVA/PAA@PEGDMA/ PEDOT:PSS hydroge	4 mm	40.61 dB	[70]
MXene/PEDOT:PSS hydrogels	4.5 mm	41 dB	[71]
ANE hydrogel	4 mm	31.5 dB	[72]
4-PG/P@CoFe Organohydroge	4 mm	50.27 dB	This Work

Infrared stealth performance of the hydrogel

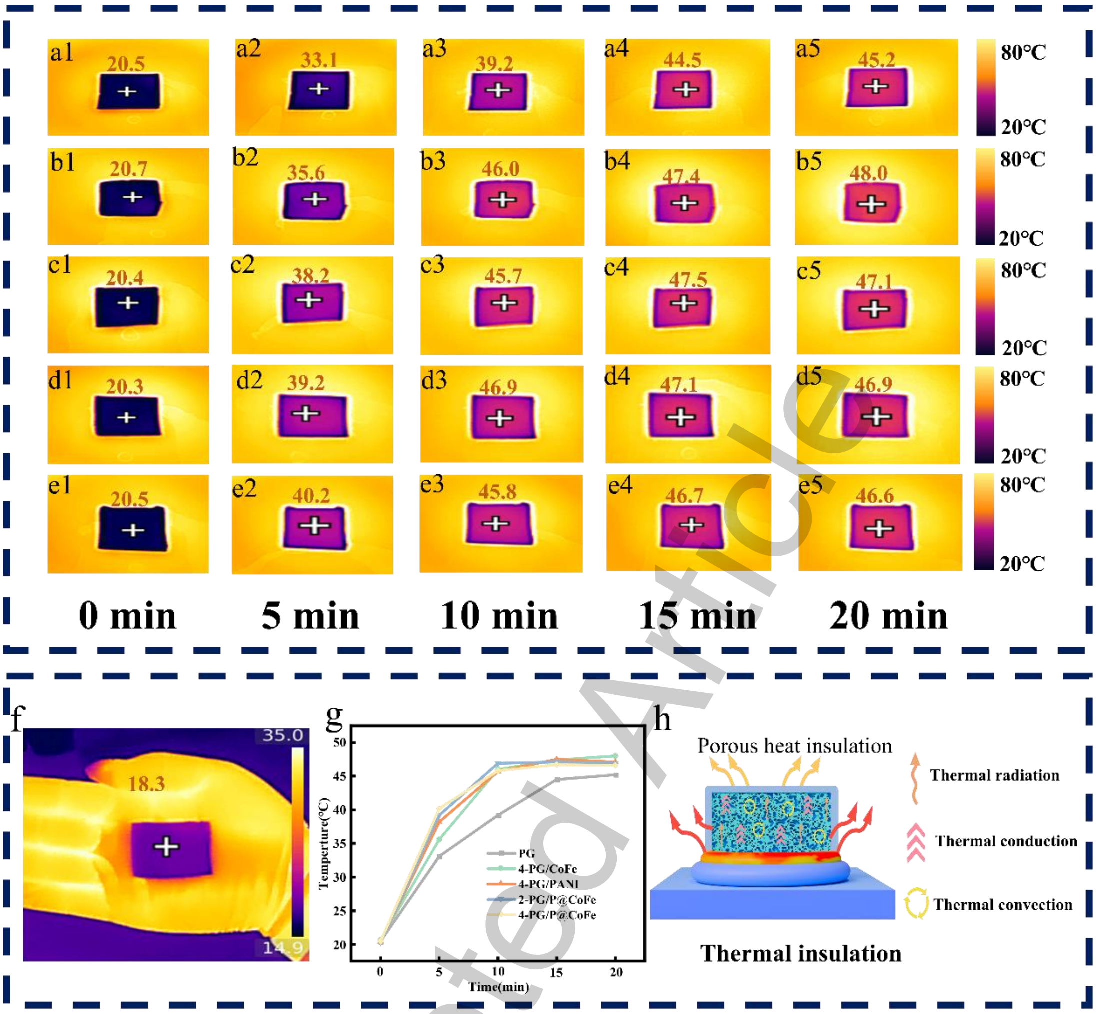

Figure 6. Evaluation of the samples' infrared stealth capabilities. (a-e) Infrared thermal images of the hydrogel samples placed on a heating plate maintained at 80 °C. (f) Infrared thermal image of the 4-PG/P@CoFe hydrogel. (g) Temperature-time curves of the sample surfaces. (h) Thermal insulation mechanism of hydrogel.

To meet the demands of more complex environments, we further evaluated the infrared stealth performance of the hydrogels. Hydrogels containing different fillers were placed on an 80 °C heating plate for 20 min, and their surface temperatures were recorded at various time intervals using an infrared thermal imaging camera. As shown in Figure 6a, the surface temperature of the hydrogel gradually increases with time. After 15 min, the equilibrium radiation temperature of the PG hydrogel stabilizes at approximately 45 °C, which is about 35 °C lower than the heating plate. This indicates that hydrogel exhibits a noticeable thermal-insulation effect. This phenomenon may be attributed to the following factors. (1) The presence of glycerol in the hydrogel slows down the evaporation rate of water and promotes the formation of a dense and stable hydrogen-bonding network within the three-dimensional gel matrix. This significantly hinders heat transfer during conduction, thereby imparting the material with a low thermal conductivity[65,73]. (2) The three-dimensional microscopic network structure of the hydrogel suppresses convective heat transfer between the material and the surrounding air[73]. It is the synergistic effect of these factors that effectively suppresses heat conduction and convection, thereby slowing the temperature rise and enabling excellent infrared stealth performance. However, it is noteworthy that after the incorporation of fillers [Figure 6b-e], the heating rate of the hydrogels increases, and the surface reaches its equilibrium radiation temperature within approximately 10 min. This is because of the contact or close packing between fillers form thermal bridges, creating continuous heat-transfer pathways that allow heat to penetrate the material more easily. However, because the heat-source intensity and surface heat-dissipation conditions remain unchanged, the system ultimately reaches thermal equilibrium at the same heat-flux balance point. As a result, the equilibrium radiation temperature shows only minor variation.

To better simulate the practical application scenario, the hydrogel was applied to the palm. As shown in Figure 6f, the infrared signal of the bare palm exhibited a distinct color contrast relative to the surrounding background. In contrast, the region covered by the hydrogel blended well with the environment and displayed a thermal signature similar to that of the surroundings, demonstrating the excellent infrared stealth capability of the hydrogel. Figures 6 g and 6 h respectively show the change in hydrogel surface temperature over time and the infrared stealth mechanism.

Sensing performance of the hydrogel

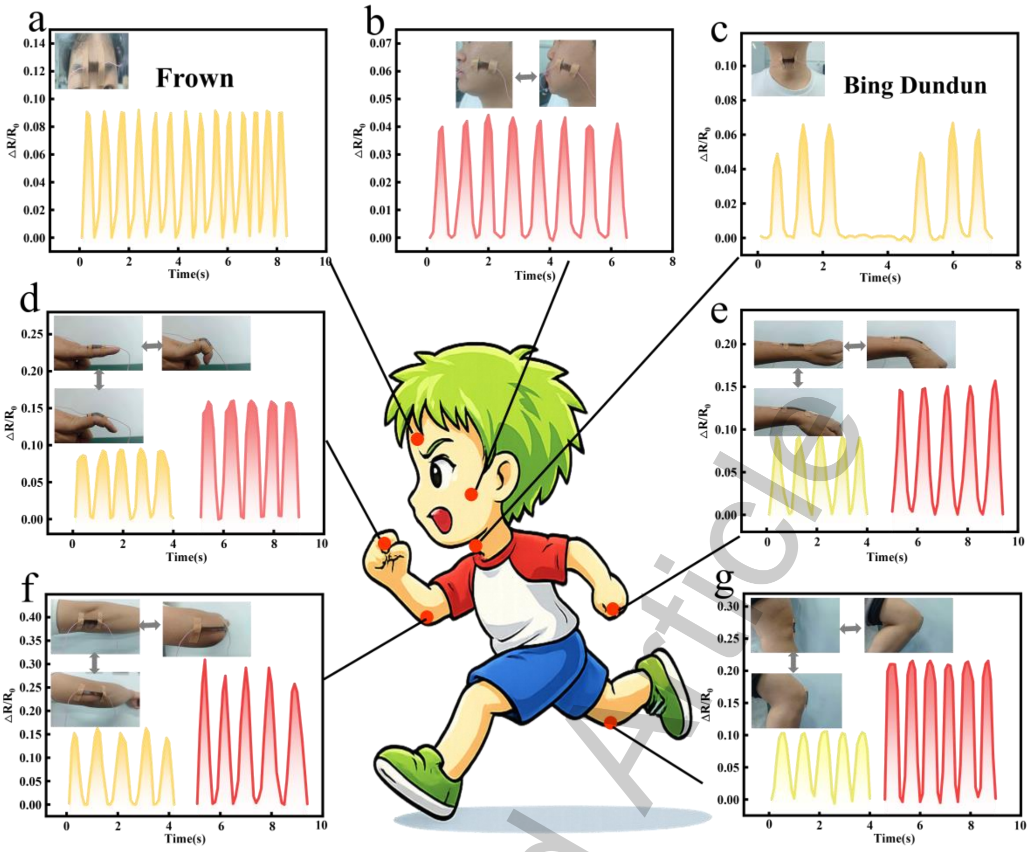

Figure 7. Real-time human-motion and physiological-signal monitoring using the 4-PG/P@CoFe hydrogel sensor. (a)Frowning. (d) Finger bending at different angles. (e) Wrist bending at different angles. (f) Elbow flexion at different angles. (g) Knee bending at different angles. All photos in the figure were taken by the author during the experiment.

As shown in Supplementary Materials Supporting Information 4, the gauge factor (GF) of 4-PG/P@CoFe exhibits a value of 2.88 over a 0%-100% strain range, demonstrating excellent linearity ($R^2 = 0.997$). This linear response is attributed to the PANI@$CoFe_2O_4$ nanoparticles, which, as conductive materials embedded within the organohydrogen network, effectively maintain the continuity of the conductive pathways under applied strain. The 4-PG/P@CoFe hydrogel, with its excellent mechanical properties, electrical conductivity, and adhesion, is highly suitable for real-time sensing and monitoring of human motion and health conditions. As shown in Figure 7, the 4-PG/P@CoFe hydrogel exhibits good linearity and sensitivity, enabling real-time detection of various strains and resistance signals generated under different motion states. It can capture subtle facial expressions in other areas, such as frowning [Figure 7a] and changes in mouth shape [Figure 7b]. When fixed on the throat [Figure 7c], the vibrations of the Adam's apple can be detected as we shout the words ‘Bing Dun Dun’, resulting in a clear and regular waveform output. Due to the Poisson effect of the hydrogel, different bending amplitudes generate distinct and regular electrical signals, as varying degrees of stretching induce different levels of network contraction and resistance change[74]. The signal intensity correlates with the magnitude of movement, enabling precise motion detection. Furthermore, the hydrogel was used to track joint motion. Figure 7d-f shows the electrical signals obtained from finger, wrist, elbow, and knee bending at various angles. These results further confirm the rapid response capability and signal stability of the 4-PG/P@CoFe hydrogel sensor under dynamic, real-time monitoring conditions. The outstanding sensing performance of the 4-PG/P@CoFe hydrogel provides a solid functional foundation for its potential applications in human motion monitoring, health management, and gesture recognition.

CONCLUSION

In summary, a multifunctional PG/P@CoFe organohydrogel was successfully fabricated by integrating conductive-magnetic PANI@$CoFe_2O_4$ nanoparticles into a PAM/Gly hydrogel network through a hydrothermal-assisted one-pot strategy. The obtained hydrogel exhibited excellent compressive properties and enhanced water-retention capability due to the incorporation of glycerol. Electromagnetic measurements revealed that, at a PANI@$CoFe_2O_4$ filler content of 4 wt.%, the 4 mm-thick hydrogels achieved an electrical conductivity of 0.55±0.01 S m^{-1} and an average EMI shielding effectiveness of 50.27±2.51 dB in the X-band. In addition, the hydrogel demonstrated excellent thermal insulation performance, together with favorable adhesion and rapid strain-responsive behavior for human-motion monitoring. This work provides an effective strategy for the development of integrated flexible materials combining strain sensing, electromagnetic shielding, and thermal management. With its multifunctionality and outstanding electromagnetic shielding performance, the hydrogel holds significant potential for applications in wearable electronic devices.

DECLARATIONS

Authors' contributions

Validation: Lei, Z.
Writing - original draft: Lei, Z.; Lu, M.
Writing - review & editing: Lei, Z.; Zhang, D.; Wang, J.; Gong, W.
Data Curation: Lu, M.; Liu, D.; Hu, Y.; Song, A.; Li, C.
Funding acquisition: Zhang, D.; Wang, J.; Gong, W.

Availability of data and materials

The data are available from the corresponding authors upon reasonable request.

AI and AI-assisted tools statement

The image of the running boy in Figure 7 was generated with the assistance of an AI-based tool and was further revised and optimized by the authors.

Financial support and sponsorship

This study was financially supported by the National Natural Science Foundation of China Project (52163001), Guizhou Provincial Science and Technology Plan Project (Qiankehe Platform Talent-GCC[2022]010-2, Qiankehe Zhongyindi [2024]042, Qiankehe Jichu-ZK[2024]YB488, Qiankehe Zhongyindi (2025)013, Qiankehe Results [2025]109,Qiankehe Talent XKBF(2025)005), Guizhou Provincial Scientist Workstation (Qiankehe Platform KXJZ[2024]022), Guizhou Provincial Department of Education 'Hundred Universities, Thousand Enterprises Science and Technology Challenge Project' (Qian Jiao Ji [2025] No. 007), Doctor Startup Fund of Guizhou Minzu University (Grant No.GZMUZK[2024]QD77)

Conflict of Interest

All authors declared that there are no conflicts of interest.

Ethical approval and consent to participate

The demonstration shown in Figure 4 and 7 involved only one of the authors as the participant and was conducted solely to demonstrate the proof-of-concept performance of the material. This test was non-invasive and did not involve any clinical procedures or the collection of sensitive personal data.

Consent for publication

Not applicable.

Copyright

REFERENCES

1. M. He, X. Zhong, X. Lu, J. Hu, K. Ruan, H. Guo, Y. Zhang, Y. Guo, J. Gu, Excellent low-frequency microwave absorption and high thermal conductivity in polydimethylsiloxane composites endowed by hydrangea-like CoNi@ BN heterostructure fillers, Advanced Materials, 36 (2024) 2410186. DOI: 10.1002/adma.202410186

2. Y. Hao, C. Liu, R. Keram, H. Song, Y. Zhang, G. Ji, Machine-learning assisted novel insulation layer stripping technology for upgrading the transparent EMI shielding materials, Nano Today, 61 (2025) 102660. DOI: 10.1016/j.nantod.2025.102660

3. M. Panahi-Sarmad, S. Samsami, A. Ghaffarkhah, S.A. Hashemi, S. Ghasemi, M. Amini, S. Wuttke, O. Rojas, K.C. Tam, F. Jiang, MOF-based electromagnetic shields multiscale design: nanoscale chemistry, microscale assembly, and macroscale manufacturing, Advanced Functional Materials, 34 (2024) 2304473. DOI: 10.1002/adfm.202470254

4. Y. Li, X. Han, J. Zhu, Y. Feng, P. Liu, X. Chen, MOF-derived Co/C-anchored MoS2-based phase change materials toward thermal management and microwave absorption, Electron, 2 (2024) e56. DOI: 10.1002/elt2.56

5. L. Wang, Y. Jiang, Y. Liu, T. Zhang, Z. Lian, Q. Li, J. Gui, D. Yu, W. Wang, Multifunctional hydrogels based on MXene/CoFe2O4 synergistically assisted rapid gelation for electromagnetic shielding, infrared stealth and wearable sensors, Chemical Engineering Journal, (2025) 167172. DOI: 10.1016/j.cej.2025.167172

6. X. Xie, M. Lu, G. Li, G. Gao, J. Kang, Q. Zhang, X. Liu, Anti-impact electromagnetic shielding hydrogel with solvent-driven tunability, Chemical Engineering Journal, 505 (2025) 159114. DOI: 10.1016/j.cej.2024.159114

7. Y. Feng, M. Qin, J. Qin, Z. Shen, X. Chen, Y. Li, R. Che, Synergistic Thermal Management and Electromagnetic Wave Absorption in Core-Sheath Phase Change Composites, Advanced Functional Materials, (2025) e23075. DOI:

10.1002/adfm.202523075
8. Q. Liu, P.-L. Wang, W. Zhang, T. Mai, M.-Y. Qi, L. Chen, J. Li, M.-G. Ma, Multifunctional wood-derived cellulose/Ti3C2Tx composite films enhanced by densification strategy for electromagnetic shielding, Joule/solar heating, and thermal camouflage, Chemical Engineering Journal, 493 (2024) 152696. DOI: 10.1016/j.jcis.2025.138103
9. T. Zhou, D. Zhang, K. Diao, J. Du, Y. Hu, Z. Lei, D. Liu, S. Liu, S. Qin, Constructing PAM/PEG electromagnetic shielding hydrogels based on MWCNTs@ TiO2, Materials Today Nano, 29 (2025) 100606. DOI: 10.1016/j.mtnano.2025.100606
10. Y. Chen, W. Guo, N. Chen, Y. Liu, X. Wan, T. Wang, Z. Zhou, Y. Jin, G. Li, Skin-inspired MXene-based polyvinyl alcohol/gelatin organic hydrogel with good anti-drying, anti-swelling properties and high sensitivity, Sensors and Actuators A: Physical, 383 (2025) 116231. DOI: 10.1016/j.sna.2025.116231
11. K.-L. Diao, D.-H. Zhang, J.-J. Du, T. Zhou, D.-J. Liu, S.-H. Qin, Electromagnetic shielding and thermal insulation hydrogels were constructed based on covalent organic skeleton COF and Ti3C2T x MXene: K.-L. Diao et al, Rare Metals, 44 (2025) 7738-7750. DOI: 10.1007/s12598-025-03436-2
12. Y. Xu, X. Zhan, J. Du, Z. Wu, D. Zhang, Fluorescent hydrogel with high toughness response based on lanthanide Metals: Material Adhesion, multicolor Modulation, information encryption, Chemical Engineering Journal, 489 (2024) 151303. DOI: 10.1016/j.cej.2024.151303
13. N. Ma, Y. Chen, L. Wang, P. Tan, N. Chen, Y. Jin, J. Song, G. Li, Ag/AgCl@ agar/P (AM-co-HEAA) hydrogel with ultra-stretchability, fatigue resistance, and freezing tolerance for human motion and electrophysiological signal monitoring, International Journal of Biological Macromolecules, (2025) 148239. DOI: 10.1016/j.ijbiomac.2025.148239
14. T. He, C. Liu, Z. Chen, C. Nie, W. Ren, Y. Zhang, H. Zhang, G. Ji, Multi-layer alternating structured alginate hydrogels featuring exceptional flexibility and electromagnetic shielding performance, Journal of Colloid and Interface Science, (2025) 138103. DOI: 10.1016/j.jcis.2025.138103
15. K. Arunprasath, P. Senthmaraikannan, I. Suyambulingam, S. Akash, S. Kathic, M.V. Chanth, N. Sunesh, Comprehensive review of advances in natural fiber composites for conductive and EMI shielding applications: Materials, mechanisms, and future prospects, International Journal of Biological Macromolecules, (2025)

145892. DOI: 10.1016/j.ijbiomac.2025.145892

16. J. Chi, S. Gu, R. Shi, R. Zhao, X. Liu, Q. Zhang, Q. Lv, Z. Xiao, L. Wang, Extending PANI molecular chains into pores of hierarchical MIL-101 as flexible electrodes for supercapacitor applications, Chemical Engineering Journal, 510 (2025) 161764. DOI: 10.1016/j.colsurfa.2024.135489

17. G. Cao, A. Wu, Z. Wang, S. Zhong, Z. Cao, H. Zhang, Enhancing the conductivity and dispersion properties of polyaniline using ethyl orange, Colloids and Surfaces A: Physicochemical and Engineering Aspects, 704 (2025) 135489. DOI: 10.1016/j.colsurfa.2024.135489

18. R. Kandpal, M. Shahadat, R. Adnan, S.W. Ali, S.Z. Ahammad, Polyaniline-based flexible nanocomposite materials, ACS Publications2022, pp. 367-395. DOI: 10.1021/bk-2022-1410.ch014

19. L.-J. Zhao, N. Tang, X.-T. Wang, M.-H. Li, J. Hu, Conductive polyaniline hydrogel featuring high toughness and low hysteresis, Chinese Journal of Polymer Science, (2025) 1-7. https://doi.org/10.1007/s10118-025-3283-0

20. M.A. Mahdy, A. Azab, I. El Zawawi, G. Turky, Tailoring ZnO/CoFe2O4 nanocomposites: structure, optical, dielectric and magnetic study, Physica Scripta, 98 (2022) 015806. DOI: 10.1088/1402-4896/aca5bc

21. R. Gholipur, Preparation and electromagnetic waves absorption performance of novel peanut shell/CoFe2O4/(RGO) x/PVA nanocomposites, Scientific Reports, 14 (2024) 30699. DOI: 10.1038/s41598-024-79286-2

22. M. Amiri, K. Eskandari, D.A. MasoudSalavati-Niasari, S. Patade, J. Kounsalye, K. Jadhav, Abraime, B., El Maalam, K., Fkhar, L., Mahmoud, A., Boschini, F., Tamerd, M. A.,... & Mounkachi, O.(2020). Influence of synthesis methods with low annealing temperature on the structural and magnetic properties of CoFe2O4 nanopowders for permanent magnet application. Journal of Magnetism and Magnetic Materials, 500, 166416, Materials Research Bulletin, 59 49-58. DOI: 10.1016/j.jmmm.2020.166416

23. M. Asandulesa, C. Hamciuc, A. Pui, C. Virlan, G. Lisa, A.I. Barzic, B. Oprisan, Cobalt ferrite/polyetherimide composites as thermally stable materials for electromagnetic interference shielding uses, International Journal of Molecular Sciences, 24 (2023) 999. DOI: 10.3390/ijms24020999

24. M. Bastianello, S. Gross, M.T. Elm, Thermal stability, electrochemical and structural characterization of hydrothermally synthesised cobalt ferrite (CoFe 2 O 4), RSC advances, 9 (2019) 33282-33289. DOI: 10.1039/c9ra06310b

25. S. Saleem, M. Irfan, M.Y. Naz, S. Shukrullah, M.A. Munir, M. Ayyaz, A.S. Alwadie, S. Legutko, J. Petrů, S. Rahman, Investigating the impact of Cu2+ doping on the morphological, structural, optical, and electrical properties of CoFe2O4 nanoparticles for use in electrical devices, Materials, 15 (2022) 3502. DOI: 10.3390/ma15103502

26. M. Afzia, R.A. Khan, B. Ismail, M.E. Zaki, T.M. Althagafi, A.A. Alanazi, A.U. Khan, Correlation between magnetic and dielectric response of CoFe2O4: Li1+/Zn2+ nanopowders having improved structural and morphological properties, Molecules, 28 (2023) 2824. DOI: 10.3390/molecules28062824

27. T. Zhou, X. Zhan, K. Diao, J. Du, Y. Xu, J. Du, R. Yang, S. Qin, D. Zhang, RGO loaded Fe3O4 strategy to construct high toughness PAM hydrogel for electromagnetic shielding, Progress in Organic Coatings, 196 (2024) 108750. DOI: 10.1016/j.porgcoat.2024.108750

28. J. Su, X. Dong, H. Zhao, C. Shi, X. Lin, Y. Xu, Y. Xie, W. Du, Dual-Loss Mechanisms in Low-Filler CoFe@ CoFe2O4/Biomass Carbon Composites for Enhanced Microwave Absorption, Colloids and Surfaces A: Physicochemical and Engineering Aspects, (2025) 137953. DOI: 10.1016/j.colsurfa.2025.137953

29. Y. Gao, X. Chen, X. Jin, C. Zhang, X. Zhang, X. Liu, Y. Li, Y. Li, J. Lin, H. Gao, Multifunction integration within magnetic CNT-bridged MXene/CoNi based phase change materials, EScience, 4 (2024) 100292. DOI: 10.1016/j.esci.2024.100292

30. J. Wang, W. Wu, W. Zhang, Y. Zhao, H. Wang, S. Yuan, J. Zhang, Synthesis, Electrical Conductivity, and Wave-Absorption Performances of Bamboo-Based Composites Co-Doped with Graphene Oxide and Polyaniline, Polymers, 17 (2024) 78. DOI: 10.3390/polym17010078

31. M. Zhao, S. Ran, X. Guo, Z. Wang, Q. Hou, Y. Liu, R. Fan, Magnetic-dielectric synergy in Fe3O4/MoS2@ polyaniline composites for high-efficiency electromagnetic wave absorption and corrosion resistance, Journal of Alloys and Compounds, (2025) 185300. DOI: 10.1016/j.jallcom.2025.185300

32. A.I.d.R. Almeida, L.d.O. Carvalho, R.C. Lopes, L.E. Sena, S.Z. do Amparo, C.P. de Oliveira, H.D. Calado, G.G. Silva, C.K. de Vasconcelos, M.M. Viana, Enhanced polyacrylamide polymer hydrogels using nanomaterials for water shutoff: Morphology, thermal and rheological investigations at high temperatures and salinity, Journal of Molecular Liquids, 405 (2024) 125041. DOI: 10.1016/j.molliq.2024.125041

33. D. Son, H. Hwang, J.F. Fontenot, C. Lee, J.P. Jung, M. Kim, Tailoring physical properties of dual-network acrylamide hydrogel composites by engineering molecular structures of the cross-linked network, ACS omega, 7 (2022) 30028-30039. DOI: 10.1021/acsomega.2c03031

34. G. Li, Y. Liu, Y. Chen, Y. Xia, X. Qi, X. Wan, Y. Jin, J. Liu, Q. He, K. Li, Robust, self-adhesive, and low-contact impedance polyvinyl alcohol/polyacrylamide dual-network hydrogel semidry electrode for biopotential signal acquisition, SmartMat, 5 (2024) e1173. DOI: 10.1002/smm2.1173

35. M. Liaskovska, Adsorption Properties of Magnetic CoFe2O4 Based Spinel Nanoparticles, International Conference on Nanotechnology and Nanomaterials, Springer, 2023, pp. 171-184. https://doi.org/10.1007/978-3-031-67519-5_13

36. T. Yun, H. Kim, A. Iqbal, Y.S. Cho, G.S. Lee, M.K. Kim, S.J. Kim, D. Kim, Y. Gogotsi, S.O. Kim, Electromagnetic shielding of monolayer MXene assemblies, Advanced Materials, 32 (2020) 1906769. DOI: 10.1002/adma.201906769

37. Y. Xia, W. Gao, C. Gao, A review on graphene-based electromagnetic functional materials: electromagnetic wave shielding and absorption, Advanced Functional Materials, 32 (2022) 2204591. DOI: 10.1002/adfm.202204591

38. K. Adamiak, A. Sionkowska, State of innovation in alginate-based materials, Marine drugs, 21 (2023) 353. DOI: 10.3390/md21060353

39. F. Wurm, B. Rietzler, T. Pham, T. Bechtold, Multivalent ions as reactive crosslinkers for biopolymers—a review, Molecules, 25 (2020) 1840. DOI: 10.3390/molecules25081840

40. D. Sharma, B. Kaith, J. Rajput, Single step in situ synthesis and optical properties of polyaniline/ZnO nanocomposites, The Scientific World Journal, 2014 (2014) 904513. DOI: 10.1155/2014/904513

41. B. Butoi, A. Groza, P. Dinca, A. Balan, V. Barna, Morphological and structural analysis of polyaniline and poly (o-anisidine) layers generated in a DC glow discharge plasma by using an oblique angle electrode deposition configuration, Polymers, 9 (2017) 732. DOI: 10.1021/acsami.2c17114

42. M. Zawrah, M. El-Okr, A. Ashery, A. Abou Hammad, Characterization of sol-gel fabricated cobalt ferrite CoFe2O4 nanoparticles, Middle East Journal of Applied Sciences, 6 (2016) 362-366. DOI: ISSN 2077-4613

43. N.T. To Loan, N.T. Hien Lan, N.T. Thuy Hang, N. Quang Hai, D.T. Tu Anh, V. Thi Hau, L. Van Tan, T. Van Tran, CoFe2O4 nanomaterials: effect of annealing

temperature on characterization, magnetic, photocatalytic, and photo-fenton properties, Processes, 7 (2019) 885. DOI: 10.3390/pr7120885

44. M. Jamil, J. Ahmad, S. Bukhari, T. Sultan, M. Akhter, H. Ahmad, G. Murtaza, Effect on structural and optical properties of Zn-substituted cobalt ferrite CoFe2O4, Journal of Ovonic Research, 13 (2017) 45-53. DOI: 10.1016/j.physb.2020.412051

45. S. Kumar, F. Ahmed, N.M. Shaalan, R. Kumar, A. Alshoaibi, N. Arshi, S. Dalela, F. Sayeed, S. Dwivedi, K. Kumari, Structural, magnetic, and electrical properties of CoFe2O4 nanostructures synthesized using microwave-assisted hydrothermal method, Materials, 15 (2022) 7955. DOI: 10.3390/ma15227955

46. R. Peng, Y. Luo, Q. Cui, H. Zhang, L. Li, Covalent organic frameworks as efficient photoinitiators and cross-linkers to fabricate highly stretchable hydrogels, ACS Applied Materials & Interfaces, 14 (2022) 49254-49263. DOI: 10.1021/acsami.2c17114

47. S. Sivaselvam, R. Selvakumar, C. Viswanathan, N. Ponpandian, Rapid one-pot synthesis of PAM-GO-Ag nanocomposite hydrogel by gamma-ray irradiation for remediation of environment pollutants and pathogen inactivation, Chemosphere, 275 (2021) 130061. DOI: 10.1016/j.chemosphere.2021.130061

48. Q. Liu, X. Kang, L. Xing, Z. Ye, Y. Yang, A facile synthesis of nanostructured CoFe 2 O 4 for the electrochemical sensing of bisphenol A, RSC advances, 10 (2020) 6156-6162. DOI: 10.1039/c9ra10936f

49. H. Jiang, Z. Feng, K. Liu, H. Wang, J. Lin, Constructing Interconnected Cofe 2 O 4/Cofe Alloyed Nanosheets for Efficient Oxygen Evolution Reaction, Available at SSRN 5297252. DOI: 10.1016/j.cej.2022.141055

50. Q. Qu, Z. Chen, G.-T. Sun, L. Qiu, M.-Q. Zhu, CoFe2O4 nanoparticles as a bifunctional agent on activated porous carbon for battery-type asymmetrical supercapacitor, Chemical Synthesis, 4 (2024) N/A-N/A. DOI: 10.20517/cs.2023.48

51. W. Rehman, F. Saeed, Y. Zhao, B. Maryam, S. Arain, M. Ayaz, A. Jamil, X. Liu, Boosted Photoelectrochemical Water Oxidation Performance with a Quaternary Heterostructure: CoFe2O4/MWCNT-Doped MIL-100 (Fe)/TiO2, Catalysts, 14 (2024) 901. DOI: 10.3390/catal14120901

52. Y.Y. Smolin, M. Soroush, K.K. Lau, Oxidative chemical vapor deposition of polyaniline thin films, Beilstein journal of nanotechnology, 8 (2017) 1266-1276. DOI: 10.3762/bjnano.8.128

53. J. Yang, X. Yu, X. Sun, Q. Kang, L. Zhu, G. Qin, A. Zhou, G. Sun, Q. Chen,

Polyaniline-decorated supramolecular hydrogel with tough, fatigue-resistant, and self-healable performances for all-in-one flexible supercapacitors, ACS applied materials & interfaces, 12 (2020) 9736-9745. DOI: 10.1021/acsami.9b20573

54. I. Dellatolas, M. Bantawa, B. Damerau, M. Guo, T. Divoux, E. Del Gado, I. Bischofberger, Local mechanism governs global reinforcement of nanofiller-hydrogel composites, ACS nano, 17 (2023) 20939-20948. DOI: 10.1021/acsnano.3c00716

55. H. Zhou, W. Cao, N. Sun, L. Jiang, Y. Liu, H. Pang, Formation mechanism and properties of NiCoFeLDH@ ZIF-67 composites, Chinese Chemical Letters, 32 (2021) 3123-3127. DOI: 10.1016/j.cclet.2021.03.050

56. C. Liu, L. Zhu, S. Zheng, L. Xu, L. Yan, Y. Zhang, G. Ji, A novel elastic dome array structure for precise pressure regulation toward tunable microwave absorption, Acta Materialia, 296 (2025) 121255. DOI: 10.1016/j.actamat.2025.121255

57. Z. Zeng, H. Jin, M. Chen, W. Li, L. Zhou, Z. Zhang, Lightweight and anisotropic porous MWCNT/WPU composites for ultrahigh performance electromagnetic interference shielding, Advanced Functional Materials, 26 (2016) 303-310. DOI: 10.1002/adfm.201503579

58. Y. Feng, G. Hai, G. Sun, K. Chen, X. Wang, J. Zhao, Y. Li, X. Chen, Dual-functional phase change composites integrating thermal buffering and electromagnetic wave absorption via multi-interfacial engineering, Advanced Fiber Materials, (2025) 1-15. DOI: 10.1007/s42765-025-00585-y

59. W. Song, S. Ness, M. Desai, J. Yi, Visible light optical coherence tomography angiography (vis-OCTA) in human retina for small vessel blood oxygenation (Conference Presentation), Ophthalmic Technologies, SPIE, 2020, pp. 112180A. https://doi.org/10.1117/12.2549090

60. W. Ouyang, L. Mei, Q. Liu, C. Ding, Y. Liu, C. Zhao, L. Xu, F. Lu, D. Luo, C. Miao, Ultrathin-flexible multifunctional MXene composite hydrogels with good mechanical properties-high strain sensitivity and ultra-broadband EMI shielding performances, Chemical Engineering Journal, 494 (2024) 153068. DOI: 10.1016/j.cej.2024.153068

61. F. Saeedi, R. Ansari, S. Sahmani, Recent advances and comprehensive review of electromagnetic interference shielding materials and technologies, Materials Today Physics, (2025) 101917. DOI: 10.1016/j.mtphys.2025.101917

62. C. Xiong, Q. Xiong, M. Zhao, B. Wang, L. Dai, Y. Ni, Recent advances in non-biomass and biomass-based electromagnetic shielding materials, Advanced

Composites and Hybrid Materials, 6 (2023) 205. DOI: 10.1007/s42114-023-00774-6

63. Z. Zeng, C. Wang, G. Siqueira, D. Han, A. Huch, S. Abdolhosseinzadeh, J. Heier, F. Nüesch, C. Zhang, G. Nyström, Nanocellulose-MXene biomimetic aerogels with orientation-tunable electromagnetic interference shielding performance, Advanced Science, 7 (2020) 2000979. DOI: 10.1016/j.polymer.2021.124101

64. Y. Zhang, K. Ruan, K. Zhou, J. Gu, Controlled distributed Ti3C2Tx hollow microspheres on thermally conductive polyimide composite films for excellent electromagnetic interference shielding, Advanced Materials, 35 (2023) 2211642. DOI: 10.1002/adma.202211642

65. H. Liu, Y. Yang, N. Tian, C. You, Y. Yang, Foam-structured carbon materials and composites for electromagnetic interference shielding: Design principles and structural evolution, Carbon, 217 (2024) 118608. DOI: 10.1016/j.carbon.2023.118608

66. Y. Yu, P. Yi, W. Xu, X. Sun, G. Deng, X. Liu, J. Shui, R. Yu, Environmentally tough and stretchable MXene organohydrogel with exceptionally enhanced electromagnetic interference shielding performances, Nano-micro letters, 14 (2022) 77. DOI: 10.1126/science.aba7977

67. X. Zhou, X.-A. Ye, J.-Q. Zhu, G.-G. Wang, Anti-drying, anti-freezing and super-elastic MXene/gelatin hydrogels for electromagnetic shielding and pressure sensing, Materials Today Physics, 53 (2025) 101709. DOI: 10.1016/j.mtphys.2025.101709

68. Y. Li, X. Xuan, Z. Pan, Y. Li, T.Q. Do, V.G. Phan, H. Chen, T. Thambi, A robust and multifunctional conductive double-network hydrogel exhibiting self-healing, anti-freezing, antibacterial, and electromagnetic shielding properties for advanced wearable sensors and biofabrication, Chemical Engineering Journal, (2025) 167264. DOI: 10.1016/j.cej.2025.167264

69. M. Shen, C. Liang, X. Xu, J. Qi, J. Sun, L. Yang, L. Xie, X. Li, Liquid metal-enhanced PVA-ANF/MXene hydrogels for electromagnetic shielding and sensing, ACS Applied Nano Materials, 7 (2024) 22158-22168. DOI: 10.1021/acsanm.4c04230

70. Z. Zhang, G. Liu, J. Wu, X. Jiang, H. Liu, Z. Li, High-strength dual-network hydrogels with chain-growth enhancement for multifunctional flexible sensors, triboelectric nanogenerators, and EMI shielding, Chemical Engineering Journal, 519 (2025) 165710. DOI: 10.1016/j.cej.2025.165710

71. P. Li, H. Wang, Z. Ju, Z. Jin, J. Ma, L. Yang, X. Zhao, H. Xu, Y. Liu, Ti3C2T x

MXene-and sulfuric acid-treated double-network hydrogel with ultralow conductive filler content for stretchable electromagnetic interference shielding, ACS nano, 18 (2024) 2906-2916. DOI: 10.1021/acsnano.3c07233

72. J. Hao, S. Hu, D. Liu, C. Yang, Y. Xu, Y. Lyu, Z. Ji, X. Wang, 3D-Printed Multifunctional Hydrogel for Integrated Electromagnetic Interference Shielding, Infrared Stealth, and Wearable Sensing, ACS Applied Materials & Interfaces, 17 (2025) 68525-68538. DOI: 10.1021/acsami.5c20335

73. Y. Li, Q. Cheng, Z. Deng, T. Zhang, M. Luo, X. Huang, Y. Wang, W. Wang, X. Zhao, Recent progress of anti-freezing, anti-drying, and anti-swelling conductive hydrogels and their applications, Polymers, 16 (2024) 971. DOI: 10.3390/polym16070971

74. J. Yang, B. Wang, Q. Zhao, K. Liu, L. Mo, H. Du, Z. Qin, X. Pan, Sustainable Conductive Organohydrogel Strengthened by Lignin@ Polypyrrole Core–Shell Nanoparticles for Multifunctional Wearable Electronics, SusMat, (2025) e70027. DOI: 10.1002/sus2.70027